Published in final edited form as:
*NMR Biomed*. 2014 December ; 27(12): 1502–1514. doi:10.1002/nbm.3127.

# 3D MR Imaging of Impaired Hyperpolarized $^{129}$Xe Uptake in a Rat Model of Pulmonary Fibrosis

**Zackary I. Cleveland**[1], **Rohan, S. Virgincar**[1,2], **Yi Qi**[1], **Scott H. Robertson**[1,3], **Simone Degan**[1,4], and **Bastiaan Driehuys**[1,2,3]

[1]Center for In Vivo Microscopy, Department of Radiology, Duke University Medical Center, Durham, NC

[2]Department of Biomedical Engineering, Duke University, Durham, NC

[3]Graduate Program in Medical Physics; Duke University Medical Center, Durham, NC

[4]Center for Molecular and Biomolecular Imaging, Duke University, Durham, NC

## Abstract

A variety of pulmonary pathologies, in particular interstitial lung diseases, are characterized by thickening of the pulmonary blood-gas barrier tissues, and this thickening results in reduced gas exchange. Such diffusive impairment is challenging to quantify spatially, because the distributions of the metabolically relevant gases ($CO_2$ and $O_2$) cannot be detected directly within the lungs. Hyperpolarized (HP) $^{129}$Xe is a promising surrogate for these metabolic gases, because MR spectroscopy and imaging allow gaseous alveolar $^{129}$Xe to be detected separately from $^{129}$Xe dissolved in the red blood cells (RBCs) and in the adjacent barrier tissues (blood plasma and lung interstitium). Further, because $^{129}$Xe reaches the RBCs by diffusing across the same barrier tissues as $O_2$barrier thickening will delay $^{129}$Xe transit and, thus, reduce RBC-specific $^{129}$Xe MR signal. Here we exploited these properties to generate 3D, MR images of $^{129}$Xe uptake by the RBCs in two groups of rats. In the experimental group, unilateral fibrotic injury was generated prior to imaging by instilling Bleomycin into one lung. In the control group, a unilateral sham instillation of saline was performed. Uptake of $^{129}$Xe by the RBCs, quantified as the fraction of RBC signal relative to total dissolved $^{129}$Xe signal, was significantly reduced ($P = 0.03$) in the injured lungs of Bleomycin-treated animals. In contrast, no significant difference ($P=0.56$) was observed between the saline-treated and untreated lungs of control animals. Together, these results indicate that 3D MRI of HP $^{129}$Xe dissolved in the pulmonary tissues can provide useful biomarkers of impaired diffusive gas exchange resulting from fibrotic thickening.

### Keywords

gas-exchange; xenon-129; interstitial lung disease; diffusion impairment; Dixon imaging; chemical shift; IPF; ILD

**Corresponding author**: Bastiaan Driehuys, Ph.D., Center for In Vivo Microscopy, Department of Radiology, Box 3302 Duke University Medical Center, Durham, NC 27710, Telephone: (919) 684-7786, Fax: (919) 684-7158, bastiaan.driehuys@duke.edu.

## INTRODUCTION

Under most circumstances, the exchange of metabolic gases (i.e., $CO_2$ and $O_2$) in the lungs is determined by pulmonary ventilation (***V***) and perfusion (***Q***)(1). Because both of these components of lung function vary spatially, it is increasingly recognized that the regional heterogeneity of ***V*** and ***Q*** and also the matching of the ***V*** and ***Q*** distributions must be characterized to fully understand pulmonary physiology in health and disease (2). To this end MR imaging—which is non-invasive, delivers no ionizing radiation, and benefits from an abundance of contrast mechanisms—has emerged as a viable modality for imaging both ventilation (3) and perfusion (4).

Although overall gas exchange in healthy individuals is predominantly determined by ***V/Q*** matching, circumstances can arise in which gas exchange is instead limited by the diffusive processes that couple ventilation and perfusion. In particular, gas exchange is impaired in a variety of pathological conditions, collectively referred to as interstitial lung disease (ILD). In ILD, the interstitial tissues between the alveoli and the capillary blood become thickened by inflammation and fibrosis, providing a physical barrier to gas diffusion (5). Moreover, inflammation and fibrosis can be spatially heterogeneous in these disorders (6), and like ventilation and perfusion abnormalities, the diffusive abnormalities resulting from ILD are also expected to be spatially heterogeneous. Thus, diagnosing and characterizing diffusive abnormalities in ILD, as well as assessing potential therapies, will likely require functional imaging.

Unfortunately, visualizing regional diffusion impairment is exceedingly challenging for two reasons: 1) interstitial thickening occurs on the scale of microns—well below the resolution of current, *in vivo* imaging modalities, and 2) $CO_2$ and $O_2$within the lungs cannot be imaged directly. It is therefore necessary to develop approaches based on non-metabolic, surrogate gases that are more amenable to imaging and possess physical properties that can be used to probe micron-scale barrier thickening. A particularly promising candidate for imaging impaired gas exchange is hyperpolarized (HP) $^{129}$Xe, which is well tolerated by human subjects (7, 8) and has already demonstrated utility for MR imaging of pulmonary microstructure (9–11) and ventilation (12–15).

Although chemically inert, $^{129}$Xe is soluble in tissues (16) and must traverse the same physical path across the pulmonary barrier tissues as $O_2$ to reach the RBCs. Once inhaled, $^{129}$Xe displays three distinct resonance peaks associated with gaseous $^{129}$Xe, $^{129}$Xe dissolved in the RBCs, and $^{129}$Xe dissolved in the adjacent barrier tissues (i.e., interstitial tissues and blood plasma). Moreover, the timescale at which non-equilibrium HP $^{129}$Xe magnetization is detected as it dissolves into the gas-exchange tissues can be varied from seconds to milliseconds. Therefore, using appropriate MR techniques, the HP $^{129}$Xe signal can be made sensitive to either pulmonary perfusion (second-timescale dynamics) or tissue-level diffusion (millisecond-timescale dynamics), depending on the experimental conditions.

Previously, these properties were exploited to visualize diffusive gas exchange both indirectly, using a technique called xenon polarization transfer contrast (XTC)(17, 18), and directly by imaging HP $^{129}$Xe magnetization as it dissolves into the gas-exchange tissues

(19–21). However, more nuanced information can be extracted by separating the total dissolved HP $^{129}$Xe signal into spectral components arising from $^{129}$Xe dissolved in the RBCs and barrier tissues. The advantage of spectrally separating the dissolved signal into RBC and barrier components was previously demonstrated in rats with Bleomycin-induced lung injury using a 2D MRI acquisition (22). Here we extend this approach to three dimensions using a 1-point variant of the Dixon technique (23), and thus provide a means to better quantify regional gas-exchange impairment. Further, we examine several quantitative metrics to characterize dissolved $^{129}$Xe images and demonstrate that one of these metrics is a promising candidate biomarker of impaired gas exchange caused by fibrotic injury.

## BACKGROUND

### Diffusing capacity of the lung

From the standpoint of classical pulmonary physiology, it may be surprising that a chemically inert gas such as HP $^{129}$Xe could be sensitive to impaired gas exchange, because it is uniformly taught that the conventional metric of gas uptake, the diffusing capacity of the lung ($\boldsymbol{D_L}$) can only be measured by reactive gases such as CO (1, 24). More specifically, the amount of gas taken up by the pulmonary tissues—conventionally given in terms of gas volume at standard temperature and pressure per unit time ($\dot{\boldsymbol{V}}$)—is typically expressed as

$$\dot{\boldsymbol{V}} = \boldsymbol{D}_L(\boldsymbol{P}_A - \boldsymbol{P}_C), \quad (1)$$

where $\boldsymbol{P_A}$ is the alveolar partial pressure of the gas, and $\boldsymbol{P_C}$ is the corresponding partial pressure in the capillary blood. Because reactive gases bind strongly to hemoglobin, the capillary RBCs serves as a nearly infinite “sink” for mass transport, and a high partial pressure gradient (i.e., $\boldsymbol{P_A} \gg \boldsymbol{P_C}$) is maintained throughout the transit time of blood through the pulmonary capillaries. Thus, gas uptake is limited only by the rate at which diffusive mass transport occurs across the alveolar membrane.

In contrast to these “diffusion limited” gases, inert gases rapidly saturate the gas-exchange membrane and, thus, cannot maintain significant partial pressure gradients. Rather, inert gas uptake is determined by blood flow away from the gas-exchange tissues, making inert gases “perfusion limited”. To reconcile this apparent discrepancy between physiological theory and empirical results demonstrating HP $^{129}$Xe’s sensitivity to pathological conditions causing impaired diffusion (22, 25–27), it is instructive to consider the physical origins of $\boldsymbol{D_L}$.

According to the classic Roughton and Forster model (28), $\boldsymbol{D_L}$ (conventional units of ml/min/mm Hg) consists of two serially ordered components and is defined by

$$\frac{\mathbf{1}}{\boldsymbol{D}_L} = \frac{\mathbf{1}}{\boldsymbol{D}_M} + \frac{\mathbf{1}}{\theta \cdot \boldsymbol{V}_c}, \quad (2)$$

where $\boldsymbol{D_M}$ is the diffusing capacity of the gas-exchange membrane; $\theta$ is the reaction rate of the gas with the blood; and $\boldsymbol{Vc}$ is the capillary blood volume. $\boldsymbol{D_M}$which will be of interest for this discussion, can be defined in terms of the physical membrane properties as (29

$$D_M = \frac{D\lambda A}{\tau}, \quad (3)$$

where $\tau$ is the membrane thickness, $D$ is the gas diffusion coefficient in the membrane, $\lambda$ is the Bunsen solubility coefficient of the gas, and $A$ is the membrane surface area. Assuming $D = 3.3\times10^{-6}$ cm$^2$/s (30), $\lambda = 1.24\times10^{-4}$ ml/ml/mm Hg [calculated from the Ostwald solubility of xenon in blood plasma (16)], $A = 2933$ cm$^2$ (31), and $\tau = 3.7 \times 10^{-5}$ cm [harmonic mean thickness of the alveolar membrane in rats (32)], the expected membrane diffusing capacity for xenon in rats is $D_{MXe} \approx 2$ ml/min/mm Hg. (Note, the diffusing capacity of the lung for xenon, $D_{LXe}$, will be less than 2 ml/min/mm Hg because the reactive component in Eq. 2 would be replaced with a second diffusive term similar to Eq. 3.

A small value for $D_{LXe}$ coupled with the vanishingly small partial pressure gradient indicates that net mass transfer into the capillary blood will be quite small. Alternately gas transfer can be considered using a more kinetic approach by calculating an approximate membrane transit time of xenon to be $\tau^2/2D \approx 2$ ms—far less than the ~3-secondtransit time of blood through the gas-exchange region in rats (33). Together, both lines of argument suggest that HP $^{129}$Xe will saturate the capillary blood almost instantaneously—exactly as expected from classical physiology.

## Uptake of non-equilibrium magnetization by the pulmonary tissues

However, it must be remembered that detecting dissolved HP $^{129}$Xe magnetization via MR methods is radically different from conventional measurements of reactive gases. That is, $D_L$ is measured at the mouth as a difference in the gas content of inspired versus expired gas. Further, it is measured on a timescale of a breath hold (~10 s). In contrast, HP $^{129}$Xe uptake is detected within the gas-exchange tissues, and this measurement can readily be performed on a timescale less than the ~100 ms needed for xenon to saturate the gas-exchange tissues (22). More importantly, whereas traditional $D_L$ measurements involve detecting partial-pressure-driven changes in gas volume, MR detects changes in the HP $^{129}$Xe magnetic moment within the gas-exchange tissues. Therefore, the relevant uptake is not driven by partial pressure gradients, but rather, by gradients in HP $^{129}$Xe magnetization. Furthermore, because of the highly non-equilibrium state of HP $^{129}$Xe, RF pulses can be exploited to maintain large magnetization gradients, even when the partial pressure of alveolar xenon has equilibrated with the blood.

As an analogy to more classical notions of gas exchange, RF excitation can be used to generate a magnetization “sink” for HP $^{129}$Xe, in a manner analogous to the sink provided by hemoglobin for reactive gases. Specifically, when using large flip angles and rapid TRs, HP $^{129}$Xe magnetization will be confined to, but never fully saturate, the gas-exchange tissues. Conversely, when using small flip angles and long TRs, sufficient HP $^{129}$Xe magnetization remains such that blood flow will have sufficient time to carry it away from the gas-exchange region. Thus, the rate at which HP $^{129}$Xe magnetization is eliminated and detected is—aside from minor hardware limitations and the physiological constraints of interest—entirely within experimental control and can act as either a perfusion limited or a diffusion limited probe depending on experimental conditions.

# EXPERIMENTAL

## Animal preparation

Two groups (Bleomycin-treated group, N = 5; saline-control group N = 4) of female Fisher rats (average weight = 170±8 g, Charles River, Wilmington, MA) were prepared for experiments following procedures approved by the Duke University Institutional Animal Care and Use Committee. Animals were first anesthetized with 55-mg/kg ketamine, positioned supine on a 45° slant board, and perorally intubated with an 18-G catheter (Abbocath-T, Hospira Venisystems, Lake Forest, IL). Through this endotracheal catheter, a PE50 catheter was placed in the right pulmonary main bronchus. Animals in the treatment group received a unilateral right lung instillation of a 0.20-ml solution of Bleomycin (3.0 units/kg body weight, Hospira, Inc. Lake Forest, IL) followed by 0.30 ml room air over a period of ~10 sec. Animals in the control group were prepared identically except that they received a 0.20 ml sham instillation of normal saline.

MR experiments were performed 25± 2 days (range 22–28 days) after treatment. Prior to MR experiments, animals were anesthetized by intraperitoneal (IP) injection of 55-mg/kg sodium pentobarbital (Nembutal, Lundbeck, Inc., Deerfield, IL), and anesthesia was maintained with periodic injections of Nembutal (15 mg/kg) administered via a 23-G IP catheter. To deliver HP $^{129}$Xe, rats were intubated with an 18-G catheter (Abbocath) to provide an airtight seal for mechanical ventilation. Animals were ventilated (75% $N_2$ and 25% $O_2$) at a rate of 1 breath/s on an HP-gas compatible, constant-volume, mechanical ventilator (34) with a tidal volume of 1.0 ml/100 g body mass. During $^{129}$Xe MR imaging and spectroscopy, $O_2$ concentration in the breathing gas mixture was kept constant, but $N_2$ was replaced with an equivalent volume of HP $^{129}$Xe. Each breath cycle comprised a 250-ms inhalation, a 50-ms breath-hold, and 750-ms of passive exhalation.

While animals were in the MR magnet, their body temperature was monitored via a rectal thermistor and maintained at ~37°C by warm air flowing through the magnet bore. Airway pressure was monitored by a pressure transducer attached to the ventilation tube. Heart rate was monitored via electrocardiogram (ECG) readings using custom Lab VIEW 8.1 software (National Instruments Corporation, Austin, TX, USA). This software also controlled the timing of the ventilator and MR acquisition.

## Lung histology and analysis

After imaging, rats were exsanguinated by opening the abdominal cavity and severing the abdominal aorta and inferior vena cava. Lungs were fixed within the thoracic cavity, by instilling 10% buffered formalin at a pressure of 25-cm $H_2O$ via the endotracheal tube for 30 minutes. Trachea, lungs, and heart were then excised en-block and stored in 10% formalin for at least 24 hours. Following fixation, lungs were cut into 5--μm thick slices, and adjacent slices were processed for hematoxylin-eosin (H&E) and Masson's trichrome staining. Both sets of stained slides were qualitatively assessed by an expert observer (S.D.), who was blinded to treatment group. Additionally, Masson's trichrome-stained slides were used to quantitatively assess collagen content as a metric of fibrotic injury, using an approach similar to that described previously (35, 36).

Briefly, 15 non-overlapping photomicrographs were obtained from each animal using a 20X objective to cover the maximum area of each lung section. Regions containing tissue at the edge of the pulmonary parenchyma, including the pleura, were excluded from selection. The level of fibrosis was calculated by applying a color threshold in ImageJ (Version 1.47t, National Institutes of Health, Bethesda, MD, http://rsb.info.nih.gov/ij/) to determine the collagen tissue area and the total tissue area in each photomicrograph. To avoid quantification bias, these areas were calculated by two automated macros that were applied identically to all photomicrographs. Collagen content was then expressed as a percent of the total tissue area. Collagen area percentages from the Bleomycin- and saline-treated groups where tested for statistical significance using a single-sided, Wilcoxon rank-sum test.

## MR and polarization hardware

Isotopically enriched xenon (83% $^{129}$Xe, in a 1% Xe, 10% $N_2$89% He mixture, Spectra Gases Inc., Alpha, NJ) was hyperpolarized by spin exchange optical pumping (37) using a prototype commercial polarizer (model 9800, MITI, Durham, NC). Following cryogenic accumulation (37), HP $^{129}$Xe (polarization~10%) was thawed into 300-ml Tedlar bags (Jensen Inert Products, Coral Springs, FL) and placed inside a Plexiglas cylinder. From this cylinder, HP $^{129}$Xe was then delivered to rats as described previously (34).

MR spectroscopy and imaging was performed at 2.0 T using a horizontal, 30-cm bore magnet (Oxford Instruments, Oxford, UK) equipped with 180-mT/m shielded gradients. This magnet was operated with a GE EXCITE 12.0 console (GE Healthcare, Milwaukee, WI) that was modified to operate at 2 T using a frequency up/down converter as described previously (38).

## MR spectroscopy

To prepare for HP$^{129}$Xe studies, rats were first ventilated with a mixture of 1% HP $^{129}$Xe flowing directly from the polarizer (39). This direct-flow $^{129}$Xe was used to localize the lungs within the field-of-view (FOV); determine the frequencies of the RBC, barrier, and gaseous $^{129}$Xe resonances; set the RF flip angle; and perform *in vivo* shimming. Direct-flow spectroscopy was also used to: 1) determine global phase offset between the RBC peak and the in-phase receiver channel and 2) the nominal echo time (TE)—defined here as the time between the end of the RF pulse and the beginning of data acquisition—required for the dissolved resonances to accumulate the 90° phase difference ($TE_{90}$) necessary for 1-point Dixon separation (22). This was accomplished by acquiring $^{129}$Xe spectra at end expiration using varying TEs [TE = 250–700 μs, 8 spectra/breath, 500 spectra total, repetition time (TR) = 75 ms, bandwidth (BW) = 8 kHz] with a selective, 1200 μs, 3-lobe sinc pulse.

Spectral data at each TE were averaged, and complex spectra were fit as a linear combination of two Lorentzians using routines written in MATLAB (Math Works, Inc., Natick, MA). The phase difference between the two dissolved $^{129}$Xe peaks was fit as function of TE, and $TE_{90}$ was determined by linear regression (see Fig. 1).

## MR imaging

Ventilation images were acquired over multiple breaths at end-expiration using a 3D radial sequence. Axial slab excitation matching the 50-mm field-of-view (FOV) was performed to avoid wraparound artifacts from HP $^{129}$Xe in the trachea. HP $^{129}$Xe was excited using a variable flip angle scheme (40) that provided constant, view-to-view MR signal intensity and consumed all available magnetization. Additional parameters included: radial views = 4291, views/breath = 20, points per view = 64, BW = 8 kHz, TR = 10 ms, and TE = 860 μs. Dissolved $^{129}$Xe images were also acquired at end-expiration using the same 3D radial sequence. Both the receiver and excitation frequencies were set on-resonance with the $^{129}$Xe RBC peak, and TE was set to the spectroscopically determined $TE_{90}$ (additional parameters: NEX = 4, FOV = 50 mm, radial views = 1073, views/breath = 8, points per view = 32, BW = 15.6 kHz, TR = 75 ms, and flip angle = 90°).

Images were reconstructed using a conjugate phase approach with the open source MATLAB toolbox of Fessler and coworkers (41). Radial k-space data was transformed into Cartesian images by a non-uniform fast Fourier transform with Min-Max interpolation (42), and each k-space data point was weighted by density compensation factors calculated via the iterative method of Pipe *et al*.(43). HP $^{129}$Xe ventilation data were reconstructed with a 64×64×64 matrix as conventional magnitude images. Dissolved $^{129}$Xe data reconstructed as magnitude images (matrix = 32×32×32) represent the total$^{129}$Xe signal originating from the gas-exchange tissues, and are referred to as ‘dissolved’ $^{129}$Xe images. Images obtained from only the real component of the dissolved $^{129}$Xe data are referred to as red blood cell (RBC) images. Similarly, images obtained from imaginary data are referred to as barrier tissue images.

## Image analysis

Image analysis was performed using routines written in MATLAB. Analysis was confined to the ventilated positions of the lung by manually segmenting the gas-phase images to create masks of the right and left lungs. Manual segmentation was also used to create masks of the trachea and other visible major airways, and these regions were omitted from further analysis. Prior to airway removal and subsequent analysis, complex dissolved $^{129}$Xe images were linearly interpolated to match the matrix size of the ventilation images. Maps of the RBC-to-barrier tissue and RBC-to-total dissolved signal distributions were generated by dividing the relevant images on a voxel-by-voxel basis. Because gas-phase and dissolved $^{129}$Xe differ substantially in $T_2$* values and potentially polarization, the ratios of the gas- and dissolved-phase signals could not be compared directly. Therefore, the total dissolved-phase images and the gas-phase images were first normalized by the sum of their respective voxel intensities before generating ‘gas-transfer’ maps of the dissolved-to-ventilation ratio distribution (19).

Differences between the Bleomycin- and saline-treated groups in the whole-lung metrics were assessed for statistical significance of using a single-sided, Wilcoxon rank-sum test. Within experimental groups, differences between the treated and untreated lungs of individual animals were assessed using one-sided, signed Wilcoxon rank-sum test. Finally,

differences between the RBC-to-barrier ratios obtained from spectroscopy and imaging were evaluated using a two-sided, signed Wilcoxon rank-sum test.

## RESULTS

### Validation of fibrotic injury

Using blinded, qualitative examination of the histology slides, all animals were correctly classified into the saline-treated or Bleomycin-treated groups. Furthermore, within the Bleomycin-treated animals, treated and untreated lungs were also correctly identified by qualitative examination. When the tissue was quantitatively assessed with Masson's Trichrome staining (see Table 1 and Fig. 2), a significantly higher percentage of collagen-containing tissue ($P = 0.008$) was observed in the Bleomycin-treated animals. These results indicate that unilateral fibrotic injury was successfully generated in all Bleomycin-treated animals, but not in saline-treated control animals.

### Spectroscopic determination of dissolved $^{129}$Xe phase evolution

In all animals, the phase difference between the RBC and barrier tissues peaks ($\Delta\phi$) evolved linearly with nominal echo time (e.g., see Fig. 1). Furthermore, the average slope derived from linear, least squares fitting of these data was 0.123±0.003°μs—in good agreement with the 0.118±0.003°μs expected from the frequency differences ($\Delta f = 328\pm9$ Hz) observed between the two peaks. However, as can be seen in Fig. 1, linear fits of phase evolution as a function of TE are also characterized by pronounced, non-zero y-intercepts that differed between animals (mean: 43±5°; range: 32–48°). Fortunately, the highly linear phase evolution of the dissolved$^{129}$Xe signal allowed the time needed to achieve the 1-point Dixon imaging condition (i.e., $TE = TE_{90}$) to be determined empirically.

### Distribution of dissolved $^{129}$Xe signal

3D images of both gaseous and dissolved $^{129}$Xe were successfully obtained from all animals (e.g., see Fig. 3). In control animals, the total dissolved$^{129}$Xe signal (i.e., intensity of the dissolved $^{129}$Xe magnitude image) within both right and left lungs tended to be higher in central regions and decreased in both the cranial and caudal directions. A similar signal intensity pattern was also observed in the corresponding ventilation images, indicating that, despite regional heterogeneity, significant matching existed between the gaseous and dissolved $^{129}$Xe signal distributions. When this relationship was examined quantitatively using the $^{129}$Xe gas-transfer ratio—defined as the normalized dissolved to normalized gas-phase signal intensity ratio (19)—a relatively narrow distribution was observed that was centered around a value of 1 (e.g., see Fig. 4a). In fact, the mean gas-transfer ratio was ~1 for all animals (see Table 1), similar to the gas-transfer values recently observed in humans (19). Further, no significant difference in mean $^{129}$Xe gas transfer was observed between the saline- and Bleomycin-treated groups ($P = 0.73$).

In fibrotic injury, the total uptake of gases by the pulmonary tissues is less straightforward to interpret than the transfer of gases from the alveolar spaces to the RBCs. Thus, the most interesting aspect of dissolved $^{129}$Xe MR is the ability to separate the total dissolved $^{129}$Xe signal into its RBC and barrier tissue components. An example of this separation, achieved

using 1-point Dixon imaging in a control animal, is shown in Fig.3c and 3d. As expected for an animal without interstitial thickening (22), $^{129}$Xe signal is observed from both the RBC and barrier tissue images throughout the ventilated region of the lungs (green outline).

A more interesting example of the transit of $^{129}$Xe gas from the alveolar spaces to the RBCs can be observed in Fig. 5, which displays the ventilation, total dissolved, RBC, and barrier tissues images from a Bleomycin-treated animal. As was seen for the control animal, there is qualitative agreement between the location of the gas-phase signal in the ventilation image and total dissolved-phase signal. However, unlike in the control animal, the central portions of the lungs do not display noticeably elevated dissolved signal relative to the lung periphery. Moreover, the $^{129}$Xe signal from the barrier is substantially mismatched with that observed from the RBC compartment, largely due to reduced RBC signal in the Bleomycin-treated, right lung.

## Comparison of HP $^{129}$Xe uptake from spectroscopy and imaging

HP$^{129}$Xe transfer metrics obtained from imaging were well correlated with their spectroscopic counterparts for all animals. That is, the image-derived, global RBC-to-barrier signal ratio (the voxel-by-voxel sum of the RBC signal divided by the voxel-by-voxel sum of the barrier tissue signal) correlated strongly with the spectroscopic RBC-to-barrier ratio ($R^2$ = 0.82, see Fig. 6). Moreover the slope of the best-fit line correlating these two metrics was near unity (1.1±0.1), and the intercept was near zero (−0.007±0.04). Together these results argue that the 1-point Dixon approach correctly captured the global signal characteristics provided by spectroscopy, while adding more nuanced, regional information.

## Regional $^{129}$Xe uptake

Somewhat surprisingly, whole-lung metrics of gas uptake, whether dissolved-to-ventilation, RBC-to-barrier, or RBC-to-dissolved, did not differentiate the saline- and Bleomycin-treated groups (see Table 1). However, examining spatial variations in the RBC-to-dissolved distribution reveals obvious differences between the saline- and Bleomycin-treated animals. For instance, Fig.7 displays representative slices from the RBC-to-dissolved maps of a saline-control (Fig. 7a) and a Bleomycin-treated animal (Fig. 7b). Specifically, the control animal displays a relatively homogeneous RBC-to-dissolved distribution in both lungs, with most values falling in the range of 0.4–0.6 and extreme values near either 0 or 1 being located primarily near the lung periphery. A similar pattern is also observed in the untreated lung of the Bleomycin-injured animal.

In contrast, substantially reduced RBC-to-dissolved values are observed throughout much of the injured, right lung. Moreover, the regional trends displayed in the RBC-to-dissolved maps are reflected in the histograms of the whole-lung, RBC-to-dissolved distributions (Fig. 7c and 7d). That is, while the control animal displays a relatively symmetric whole-lung RBC-to-dissolved distribution similar to the one seen in Fig. 4c, the Bleomycin-treated animal displays a left-skewed distribution, indicating that regions of the lung experienced reduced $^{129}$Xe transfer to the RBCs on the TR = 75-ms timescale.

In Bleomycin-treated animals, the average RBC-to-dissolved ratio was significantly reduced in the treated versus untreated lung (P = 0.03, see Fig. 8a). Moreover, in no instance was the

opposite pattern observed within the injured lung (i.e., higher mean RBC-to-dissolved ratio relative to the untreated lung) for any of the Bleomycin-treated animals. In contrast, the saline-treated animals displayed no significant difference in RBC-to-dissolved distribution between the saline-treated and untreated lungs (P = 0.31, Fig. 8a). Together, these results are in excellent agreement with the expectation that exposing a lung to Bleomycin would generate fibrotic thickening, resulting in reduced gas transport to the RBCs.

Beyond the mean RBC-to-dissolved values, it is interesting to investigate the heterogeneity of the RBC-to-dissolved distribution. Fig. 8b displays a comparison of the heterogeneity, as measured by the coefficient of variation (CV), in the treated versus untreated lungs for both the saline- and Bleomycin-treated groups. In all Bleomycin-treated animals the CV of the RBC-to-dissolved distribution was significantly higher in the treated versus untreated lungs (P = 0.03). However, in the saline control animals, no significant difference in CV was observed for the RBC-to-dissolved (P = 0.56) distribution between the treated and untreated lungs. Together, these results suggest that, compared to both untreated and saline treated lungs, the presence of fibrotic tissue in Bleomycin-treated lungs reduced $^{129}$Xe exchange and increased its spatial heterogeneity.

## DISCUSSION

### Implications of non-TE-dependent phase evolution

The accumulation of phase differences between the two dissolved $^{129}$Xe resonances increased linearly with the product of the frequency difference between the two peaks, Δf, and TE. This observation, despite the known rapid diffusive$^{129}$Xe exchange (44), suggests that the pre-imaging spectroscopy protocol used in this work could be simplified by acquiring a single spectrum to measure Δf and, using this information, calculate $TE_{90}$.

However, plots of Δϕ vs. TE, while showing excellent linearity, also exhibited pronounced, non-zero intercepts. As a result, naively using the measured Δf to calculate $TE_{90}$ will not yield the expected phase shift. In fact, to do so in this work would have led to phase offsets that exceeded 90° by 36–53% (total phase evolution 122–138°). In turn, this excess phase accumulation would have prevented meaningful separation of the RBC and barrier components of the $^{129}$Xe signal and thus, prevented the regions in which gas-exchange was impaired from being correctly identified.

Because the phase difference between the two dissolved $^{129}$Xe resonances cannot be attributed solely to TE, substantial phase evolution must also have occurred during the RF pulse. Furthermore, such an effect is consistent with the RF-induced phase contrast observed in the ultra-short echo time (UTE) imaging of connective tissues (45). However, unlike the case of $^{1}$H-based structural UTE imaging, RF-induced phase evolution cannot be avoided when exciting dissolved HP $^{129}$Xe simply by using small flip angle, hard pulses. That is, to generate sufficient dissolved $^{129}$Xe signal intensity and to confine its magnetization to the gas-exchange tissues (20, 21), large flip angle RF pulses are required. Additionally, these RF pulses must be relatively long (~1 ms), so that they are sufficiently selective to avoid exciting the 100-fold larger magnetization pool present in the gas phase. Thus, RF-induced phase evolution is likely an unavoidable complication when using TE-dependent phase

evolution to separate the RBC and barrier tissue components of the dissolved $^{129}$Xe signal. Note that this complication will be present regardless of whether Dixon-based (22) or conventional IDEAL-based (46) approaches are used to achieve this spectral separation. However, in future work, it may be possible to model RF-induced phase evolution using a rigorous treatment of the Bloch equations.

### Choice of dissolved $^{129}$Xe distribution

It is not obvious *a priori* how best to transform the dissolved $^{129}$Xe image data into meaningful metrics of regional gas uptake. That is, the HP $^{129}$Xe signal originating from the lungs can be conceptually divided into: 1) the total dissolved-phase, which comprises 2) $^{129}$Xe dissolved in the RBCs, and 3) $^{129}$Xe dissolved barrier tissues, and finally 4) the gas-phase, which serves as the magnetization source for the dissolved-phase components. Thus, it is ambiguous as to which of these interrelated measures of pulmonary HP $^{129}$Xe magnetization should be directly compared. Intuitively, regional variations in gas uptake could be assessed by calculating the ratio of two out of the four interrelated $^{129}$Xe components, for instance: the total dissolved-to-gas-phase, barrier tissue-to-gas-phase, RBC-to-gas-phase, and RBC-to-barrier tissue ratios (46).

However, direct comparisons between the gas- and dissolved-phase signals is complicated by a 10-fold difference in $T_2$* between the two phases (47) and is further complicated in this work, because gas- and dissolved-phase images were acquired as separate images. The RBC-to-barrier tissue ratio avoids both complications, because the RBC and barrier data are derived from the same acquisition, and because the $T_2$* is similar for both components. However, as can be seen in Fig. 4b, the RBC-to-barrier distribution is highly skewed to the left, making it difficult to calculate meaningful summary statistics, and thus complicating comparisons between different animals.

One possible approach for transforming the RBC-to-barrier distribution into a more statistically tractable form is to use signal-intensity-based thresholding and segmentation to eliminate regions with low barrier tissue signal such as the heart and larger vasculature (46). However, if a sufficiently large flip angle RF pulse and rapid TRs are used in the image acquisition (e.g., the 75 ms TR and 90° pulse used in this work), HP $^{129}$Xe magnetization in these “down stream” regions will be eliminated by RF-induced depolarization during image acquisition. Therefore, the appearance of high RBC-to-barrier tissue values in Fig. 4b (and indeed, in the RBC-to-barrier tissue distributions of all animals studied in this work) indicate that at least in some instances, high RBC-to-barrier tissue ratios reflect physiologically meaningful data. Furthermore, the Ostwald solubility of xenon in RBCs is ~3-fold higher than in blood plasma (16), suggesting that regions displaying RBC-to-barrier ratios >1 are indeed quite plausible.

To retain gas-exchange information from regions with reduced barrier signal, we examined$^{129}$Xe gas uptake via the RBC-to-total dissolved ratio. This metric ultimately contains the same information as the RBC-to-barrier ratio, but the resulting distributions are much less skewed (e.g., see Fig. 4c) and innately constrained to values ranging from 0–1. This makes the RBC-to-dissolved ratio more amenable to statistical analysis. Moreover, this metric should also be more robust against imperfect separation of the RBC and barrier

signals than the RBC-barrier-ratio, where experimental errors are present with opposite sign in both the numerator and denominator, thus compounding experimental error. In contrast, separation error is only present in the numerator of the RBC-to-dissolved ratio. Together, these features make the RBC-to-dissolved ratio a more promising candidate for being a useful biomarker of impaired gas exchange than the RBC-barrier-ratio.

### Global imaging metrics and regional injury

Previous spectroscopic studies demonstrated diminished RBC relative to barrier tissue signal in rats subjected to pulmonary injury with lipopolysaccharide (LPS) (26), infected with Stachybotrys chartarum (27), and exposed to Bleomycin (22). Thus, it is interesting to note that the whole-lung metrics obtained in this work, whether derived from spectroscopy or imaging (see Table 1), did not statistically differentiate the Bleomycin and saline treated groups. However, both the fungal infection and the LPS were acute insults that elicit substantial, and ongoing, inflammatory responses. Similarly, the Bleomycin-injured animals reported previously (22) were imaged much sooner (10.6±4.0 days) after injury compared to our current work, in which animals were imaged ~1 month after injury. This timing is relevant, because Bleomycin injury involves an initial inflammatory stage that, in rats, does not fully subside into the fibrotic stage until after approximately 21 days after injury (48, 49). Thus, it likely that the earlier $^{129}$Xe/Bleomycin study was conducted during a primarily inflammatory stage, whereas our current study assessed the fibrotic phase of injury.

Together, these observations suggest a possible origin for the apparent discrepancy between the whole-lung data of this and earlier works. Previous studies of pulmonary perfusion using computed tomography (CT) have demonstrated that blood flow is preferentially redistributed to inflamed regions within the lungs (50). However, these inflamed regions are expected to display the more pronounced gas exchange impairment relative to non-inflamed regions. Thus, this combination of increased blood flow and impaired gas exchange within the inflamed regions likely reduced the RBC-to-barrier tissue ratio in the injured animals. Regardless of the mechanism causing the discrepancy between whole-lung observations in this and previous studies, Figs. 5, 7, and 8 clearly indicate that 3D, 1-point Dixon imaging of dissolved $^{129}$Xe can correctly identify fibrotic regions of the lungs where gas exchange is impaired. Moreover, this discrepancy between regional and global information clearly highlights the need to resolve gas exchange regionally when quantifying diffusion impairment in these models.

### Study limitations

Ventilation images were manually segmented, which may have introduced subjectivity into the image analysis. Furthermore, restricting analysis to only the ventilated regions made the approach insensitive to injury-induced ventilation defects, which will also play a role in overall gas exchange. Fortunately, both issues could be avoided in future work using a dual-tuned $^{1}$H/$^{129}$Xe coil to acquire $^{1}$H images of the thoracic cavities, and then using these anatomic images to define regions of interest for quantitative analysis (51).

Additionally, several assumptions were made in applying 1-point Dixon imaging: 1) $B_0$is homogeneous across the lungs, 2) chemical shift-induced phase evolution during acquisition

is negligible, and 3) differential, off-resonance phase evolution under magnetic field gradients is also negligible. Assumption 1 is likely valid, because the short TEs used will have made the imaging relatively robust to the minor $B_0$ variation expected in a preclinical magnet. The 2nd and 3rd assumptions are more problematic, because some degree of phase evolution must occur during the ~1-ms data acquisition period, and gradient-induced, off-resonance dephasing is known to contribute to the phase contrast observed in UTE imaging (45). However, RBC signal was only reduced in the injured lungs, suggesting that this 3D, 1-point Dixon approach captured the key features of diffusive exchange and any additional phase evolution contributed only secondary blurring effects.

Perhaps the greatest limitation of the methods presented in the current study, and indeed virtually all HP gas-derived metrics reported to date, is that that they yield only semi-quantitative information about pulmonary function. That is, while the ratios reported in this here enable statistical comparisons to be made between individuals and between the lungs of a given subject, these metrics lack the conventional units (e.g., ml/min/g or ml/min/mm Hg) used in the physiological literature. Fortunately, several quantitative models that account for both blood flow and diffusion have been developed to describe HP $^{129}$Xe uptake by the gas-exchange tissues (22, 25, 52). With proper development, it should be possible to adapt these models such that they can provide regional metrics of both normal and pathological pulmonary gas exchange.

## CONCLUSIONS

We have described a 3DMR imaging approach that allows HP $^{129}$Xe in the alveolar spaces to be detected separately from $^{129}$Xe dissolved in both the red blood cells and the barrier tissues of the lungs of small animals. By applying RF pulses with sufficiently large flip angle and short repetition time, the dissolved signal can be almost exclusively confined to the gas-exchange tissues, making this imaging approach sensitive to diffusive impairment caused by fibrotic thickening of the barrier tissues. Additionally, we have demonstrated that regional differences in diffusive $^{129}$Xe exchange are readily detected by the RBC-to-total dissolved signal ratio, a metric that is readily amenable to statistical analysis. If implemented in transgenic mice that exclusively express human hemoglobin (53), this approach can be extended to a wide variety of preclinical models of human disease. Moreover, a single breath variant of this technique could enable clinical investigations of gas-exchange impairment in patients, providing a unique method to evaluate the efficacy of therapeutic agents in human diseases that involve impaired gas diffusion, such as idiopathic pulmonary fibrosis.

## Acknowledgments

This study was funded by the National Institutes of Health (NHLBI R01HL105643, NCI R01-CA-142842, and NHLBI 1K99-HL-111217-01A1) and performed at the Duke Center for In Vivo Microscopy, a National Biomedical Technology Resource Center (NIBIB P41 EB015897). The authors wish to thank Laurence Hedlund for suggestions regarding experimental design; Judith Voynow and Bernard Fischer for providing access to the microscope used for histology; Gary Cofer and Sally Gewalt for assistance with image reconstruction and acquisition; S. Sivaram Kaushik and Matthew Freeman for helpful discussions regarding data analysis; and Sally Zimney for proofreading the manuscript.

**Research Sponsors**

This study was funded by National Institutes of Health (NHLBI R01HL105643, NHLBI 1K99-HL-111217-01A1, and NCI R01-CA-142842) and performed at the Duke Center for In Vivo Microscopy, a National Biomedical Technology Resource Center (NIBIB P41 EB015897).

## Non-standard Abbreviations

| | |
|---|---|
| **CV** | Coefficient of variation |
| **$D_L$** | Diffusing capacity of the lung |
| **$D_M$** | Membrane diffusing capacity of the lung |
| **Δf** | Frequency difference between red blood cell and barrier tissue resonances of dissolved $^{129}Xe$ |
| **Δϕ** | Phase difference between red blood cell and barrier tissue resonances of $^{129}Xe$ |
| **HP** | Hyperpolarized |
| **ILD** | Interstitial lung disease |
| **RBC** | Red blood cell |
| **$TE_{90}$** | Nominal echo time needed for RBC and barrier tissue resonances to achieve a 90° phase separation |
| **UTE** | Ultra-short echo time |

## REFERENCES

1. West, JB. Respiratory Physiology: The Essentials. 9th ed. Baltimore, MD: Lippincott Williams & Wilkins; 2012.
2. Robertson HT, Buxton RB. Imaging for lung physiology: What do we wish we could measure? J. Appl. Physiol. 2012; 113(2):317–327. [PubMed: 22582217]
3. Fain S, Schiebler ML, McCormack DG, Parraga G. Imaging of Lung Function Using Hyperpolarized Helium-3 magnetic resonance imaging: Review of current and emerging translational methods and applications. J. Magn. Reson. Imaging. 2010; 32(6):1398–1408. [PubMed: 21105144]
4. Hopkins SR, Prisk GK. Lung perfusion measured using magnetic resonance imaging: New tools for physiological insights into the pulmonary circulation. J. Magn. Reson. Imaging. 2010; 32(6):1287–1301. [PubMed: 21105135]
5. Hegewald MJ. Diffusing capacity. Clin. Rev. Allergy Immunol. 2009; 37(3):159–166. [PubMed: 19330553]
6. Fishbein MC. Assessing the role of surgical lung biopsy in the diagnosis of idiopathic pulmonary fibrosis. Chest. 2005; 128(5):520S–525S. [PubMed: 16304242]
7. Shukla Y, Wheatley A, Kirby M, Svenningsen S, Farag A, Santyr GE, Paterson NAM, McCormack DG, Parraga G. Hyperpolarized Xe-129 magnetic resonance imaging: Tolerability in healthy volunteers and subjects with pulmonary disease. Acad. Radiol. 2012; 19(8):941–951. [PubMed: 22591724]
8. Driehuys B, Martinez-Jimenez S, Cleveland ZI, Metz GM, Beaver DM, Nouls JC, Kaushik SS, Firszt R, Willis C, Kelly KT, Wolber J, Kraft M, McAdams HP. Chronic Obstructive Pulmonary Disease: Safety and tolerability of hyperpolarized Xe-129 MR imaging in healthy volunteers and patients. Radiology. 2012; 262(1):279–289. [PubMed: 22056683]
9. Kaushik SS, Cleveland ZI, Cofer GP, Metz G, Beaver D, Nouls J, Kraft M, Wolber J, Kelly KT, Auffermann W, McAdams HP, Driehuys B. Diffusion weighted imaging of hyperpolarized 129Xe in patients with chronic obstructive pulmonary disease. Magn. Reson. Med. 2011; 65(4):1154–1165. [PubMed: 21413080]

10. Mata JF, Altes TA, Cai J, Ruppert K, Mitzner W, Hagspiel KD, Patel B, Salerno M, Brookeman JR, de Lange EE, Tobias WA, Wang HTJ, Cates GD, Mugler JP. Evaluation of emphysema severity and progression in a rabbit model: comparison of hyperpolarized He-3 and Xe-129 diffusion MRI with lung morphometry. J. Appl. Physiol. 2007; 102(3):1273–1280. [PubMed: 17110518]
11. Boudreau M, Xu XJ, Santyr GE. Measurement of 129Xe gas apparent diffusion coefficient anisotropy in an elastase-instilled rat model of emphysema. Magn. Reson. Med. 2013; 69(1):211–220. [PubMed: 22378050]
12. Virgincar RS, Cleveland ZI, Kaushik SS, Freeman MS, Nouls J, Cofer G, Martinez-Jimenez S, He M, Kraft M, Wolber J, McAdams HP, Driehuys B. Quantitative analysis of hyperpolarized 129Xe ventilation imaging in healthy volunteers and subjects with chronic obstructive pulmonary disease. NMR Biomed. 2013; 26(4):424–435. [PubMed: 23065808]
13. Kirby M, Svenningsen S, Kanhere N, Owrangi A, Wheatley A, Coxson HO, Santyr GE, Paterson NAM, McCormack DG, Parraga G. Pulmonary ventilation visualized using hyperpolarized helium-3 and xenon-129 magnetic resonance imaging: differences in COPD and relationship to emphysema. J. Appl. Physiol. 2013; 114(6):707–715. [PubMed: 23239874]
14. Kirby M, Svenningsen S, Owrangi A, Wheatley A, Farag A, Ouriadov A, Santyr GE, Etemad-Rezai R, Coxson HO, McCormack DG, Parraga G. Hyperpolarized He-3 and Xe-129 MR imaging in healthy volunteers and patients with chronic obstructive pulmonary disease. Radiology. 2012; 265(2):600–610. [PubMed: 22952383]
15. Mugler JP, Driehuys B, Brookeman JR, Cates GD, Berr SS, Bryant RG, Daniel TM, deLange EE, Downs JH, Erickson CJ, Happer W, Hinton DP, Kassel NF, Maier T, Phillips CD, Saam BT, Sauer KL, Wagshul ME. MR imaging and spectroscopy using hyperpolarized Xe-129 gas: Preliminary human results. Magn. Reson. Med. 1997; 37(6):809–815. [PubMed: 9178229]
16. Chen RYZ, Fan FC, Kim S, Jan KM, Usami S, Chien S. Tissue-blood partition-coefficient for Xenon: Temperature and hematocrit dependence. J. Appl. Physiol. 1980; 49(2):178–183. [PubMed: 7400000]
17. Ruppert K, Brookeman JR, Hagspiel KD, Mugler JP. Probing lung physiology with xenon polarization transfer contrast (XTC). Magn. Reson. Med. 2000; 44(3):349–357. [PubMed: 10975884]
18. Dregely I, Ruset IC, Mata JF, Ketel J, Ketel S, Distelbrink J, Altes TA, Mugler JP, Miller GW, Hersman FW, Ruppert K. Multiple-exchange-time xenon polarization transfer contrast (MXTC) MRI: Initial results in animals and healthy volunteers. Magn. Reson. Med. 2012; 67(4):943–953. [PubMed: 22213334]
19. Kaushik SS, Freeman MS, Cleveland ZI, Davies J, Stiles J, Virgincar RS, Robertson SH, He M, Kelly KT, Foster WM, McAdams HP, Driehuys B. Probing the regional distribution of pulmonary gas exchange through single-breath gas-and dissolved-phase Xe-129 MR imaging. J. Appl. Physiol. 2013; 115(6):850–860. [PubMed: 23845983]
20. Cleveland ZI, Cofer GP, Metz G, Beaver D, Nouls J, Kaushik SS, Kraft M, Wolber J, Kelly KT, McAdams HP, Driehuys B. Hyperpolarized Xe-129 MR imaging of alveolar gas uptake in humans. PLoS One. 2010; 5(8):e12192. [PubMed: 20808950]
21. Mugler JP, Altes TA, Ruset IC, Dregely IM, Mata JF, Miller GW, Ketel S, Ketel J, Hersman FW, Ruppert K. Simultaneous magnetic resonance imaging of ventilation distribution and gas uptake in the human lung using hyperpolarized xenon-129. Proc. Natl. Acad. Sci. U.S.A. 2010; 107(50): 21707–21712. [PubMed: 21098267]
22. Driehuys B, Cofer GP, Pollaro J, Mackel JB, Hedlund LW, Johnson GA. Imaging alveolar-capillary gas transfer using hyperpolarized Xe-129 MRI. Proc. Natl. Acad. Sci. U.S.A. 2006; 103(48):18278–18283. [PubMed: 17101964]
23. Ma JF. Dixon techniques for water and fat imaging. J. Magn. Reson. Imaging. 2008; 28(3):543–558. [PubMed: 18777528]
24. Forster, RE. Diffusion of Gases Across the Alveolar Membrane. Comprehensive Physiology. John Wiley & Sons, Inc; 2011.
25. Patz S, Muradyan I, Hrovat MI, Dabaghyan M, Washko GR, Hatabu H, Butler JP. Diffusion of hyperpolarized 129Xe in the lung: A simplified model of 129Xe septal uptake and experimental results. New J. Phys. 2011; 13:015009.

26. Mansson S, Wolber J, Driehuys B, Wollmer P, Golman K. Characterization of diffusing capacity and perfusion of the rat lung in a lipopolysaccaride disease model using hyperpolarized Xe-129. Magn. Reson. Med. 2003; 50(6):1170–1179. [PubMed: 14648564]
27. Abdeen N, Cross A, Cron G, White S, Rand T, Miller D, Santyr G. Measurement of xenon diffusing capacity in the rat lung by hyperpolarized 129Xe MRI and dynamic spectroscopy in a single breath-hold. Magn. Reson. Med. 2006; 56(2):255–264. [PubMed: 16767751]
28. Roughton FJW, Forster RE. Relative importance of diffusion and chemical reaction rates in determining rate of exchange of gases in the human lung, with special reference to true diffusing capacity of pulmonary membrane and volume of blood in the lung capillaries. J. Appl. Physiol. 1957; 11(2):290–302. [PubMed: 13475180]
29. Weibel ER, Federspiel WJ, Fryderdoffey F, Hsia CCW, Konig M, Staldernavarro V, Vock R. Morphometric model for pulmonary diffusing-capacity .1. Membrane diffusing-capacity. Resp. Physiol. 1993; 93(2):125–149.
30. Ruppert K, Mata JF, Brookeman JR, Hagspiel KD, Mugler JP. Exploring lung function with hyperpolarized Xe-129 nuclear magnetic resonance. Magn. Reson. Med. 2004; 51(4):676–687. [PubMed: 15065239]
31. Massaro GD, Mortola JP, Massaro D. Estrogen modulates the dimensions of the lung's gas-exchange surface area and alveoli in female rats. Am. J. Physiol-Lung C. 1996; 270(1):L110–L114.
32. Weibel ER. Morphometric estimation of pulmonary diffusion capacity .5. Comparative morphometry of alveolar lungs. Resp. Physiol. 1972; 14(1–2):26–43.
33. Presson RG, Todoran TM, DeWitt BJ, McMurtry IF, Wagner WW. Capillary recruitment and transit time in the rat lung. J. Appl. Physiol. 1997; 83(2):543–549. [PubMed: 9262451]
34. Nouls J, Fanarjian M, Hedlund L, Driehuys B. A Constant-volume ventilator and gas recapture system for hyperpolarized gas MRI of mouse and rat lungs. Conc. Magn. Reson. B. 2011; 39B(2): 78–88.
35. Lin R, Degan S, Theriot BS, Fischer BM, Strachan RT, Liang JR, Pierce RA, Sunday ME, Noble PW, Kraft M, Brody AR, Walker JKL. Chronic treatment in vivo with beta-adrenoceptor agonists induces dysfunction of airway beta(2)-adrenoceptors and exacerbates lung inflammation in mice. Brit. J. Pharmacol. 2012; 165(7):2365–2377. [PubMed: 22013997]
36. Fischer BM, Wong JK, Degan S, Kummarapurugu AB, Zheng S, Haridass P, Voynow JA. Increased expression of senescence markers in cystic fibrosis airways. Am. J. Physiol-Lung C. 2013; 304(6):L394–L400.
37. Driehuys B, Cates GD, Miron E, Sauer K, Walter DK, Happer W. High-volume production of laser-polarized Xe-129. Appl. Phys. Let. 1996; 69(12):1668–1670.
38. Cleveland ZI, Moller HE, Hedlund LW, Nouls JC, Freeman MS, Qi Y, Driehuys B. In vivo MR imaging of pulmonary perfusion and gas exchange in rats via continuous extracorporeal infusion of hyperpolarized 129Xe. PLoS One. 2012; 7(2):e12192.
39. Driehuys B, Pollaro J, Cofer GP. In vivo MRI using real-time production of hyperpolarized Xe-129. Magn. Reson. Med. 2008; 60(1):14–20. [PubMed: 18581406]
40. Zhao L, Mulkern R, Tseng CH, Williamson D, Patz S, Kraft R, Walsworth RL, Jolesz FA, Albert MS. Gradient-echo imaging considerations for hyperpolarized Xe-129 MR. J. Magn. Reson. B. 1996; 113(2):179–183.
41. Fessler JA. Matlab tomography toolbox. http://www.eecs.umich.edu/~fessler.
42. Fessler JA, Sutton BP. Nonuniform fast Fourier transforms using min-max interpolation. IEEE Trans. Signal Proces. 2003; 51(2):560–574.
43. Pipe JG, Menon P. Sampling density compensation in MRI: Rationale and an iterative numerical solution. Magn. Reson. Med. 1999; 41(1):179–186. [PubMed: 10025627]
44. Bifone A, Song YQ, Seydoux R, Taylor RE, Goodson BM, Pietrass T, Budinger TF, Navon G, Pines A. NMR of laser-polarized xenon in human blood. Proc. Natl. Acad. Sci. U.S.A. 1996; 93(23):12932–12936. [PubMed: 8917521]
45. Carl M, Chiang JTA. Investigations of the origin of phase differences seen with ultrashort TE imaging of short T2 meniscal tissue. Magn. Reson. Med. 2012; 67(4):991–1003. [PubMed: 21898582]

46. Qing K, Ruppert K, Jiang Y, Mata JF, Miller GW, Shim YM, Wang C, Ruset IC, Hersman FW, Altes TA, Mugler JP. Regional mapping of gas uptake by blood and tissue in the human lung using hyperpolarized xenon-129 MRI. J. Magn. Reson. Imaging. 2013
47. Mugler, JP.; Altes, TA.; Ruset, IC.; Miller, GW.; Mata, JF.; Qing, K.; Tsentalovich, I.; Hersman, FW.; Ruppert, K. Image-based measurement of T2* for dissolved-phase Xe129 in the human lung. Proceedings of the 20th Annual Meeting of the ISMRM; Salt Lake City, UT, USA. 2012. p. 1347
48. Babin AL, Cannet C, Gerard C, Wyss D, Page CP, Beckmann N. Noninvasive assessment of bleomycin-induced lung injury and the effects of short-term glucocorticosteroid treatment in rats using MRI. J. Magn. Reson. Imaging. 2011; 33(3):603–614. [PubMed: 21563244]
49. Chaudhary NI, Schnapp A, Park JE. Pharmacologic differentiation of inflammation and fibrosis in the rat bleomycin model. American Journal of Resp. Crit. Care Med. 2006; 173(7):769–776.
50. Fuld MK, Halaweish AF, Haynes SE, Divekar AA, Guo JF, Hoffman EA. Pulmonary perfused blood volume with dual-energy CT as surrogate for pulmonary perfusion assessed with dynamic multidetector CT. Radiology. 2013; 267(3):747–756. [PubMed: 23192773]
51. Kirby M, Heydarian M, Svenningsen S, Wheatley A, McCormack DG, Etemad-Rezai R, Parraga G. Hyperpolarized He-3 magnetic resonance functional imaging semiautomated segmentation. Acad. Radiol. 2012; 19(2):141–152. [PubMed: 22104288]
52. Chang YLV. MOXE: A model of gas exchange for hyperpolarized 129Xe magnetic resonance of the lung. Magn. Reson. Med. 2013; 69(3):884–890. [PubMed: 22565296]
53. Freeman MS, Cleveland ZI, Qi Y, Driehuys B. Enabling hyperpolarized 129Xe MR spectroscopy and imaging of pulmonary gas transfer to the red blood cells in transgenic mice expressing human hemoglobin. Magn. Reson. Med. 2013; 70(5):1192–1199. [PubMed: 24006177]

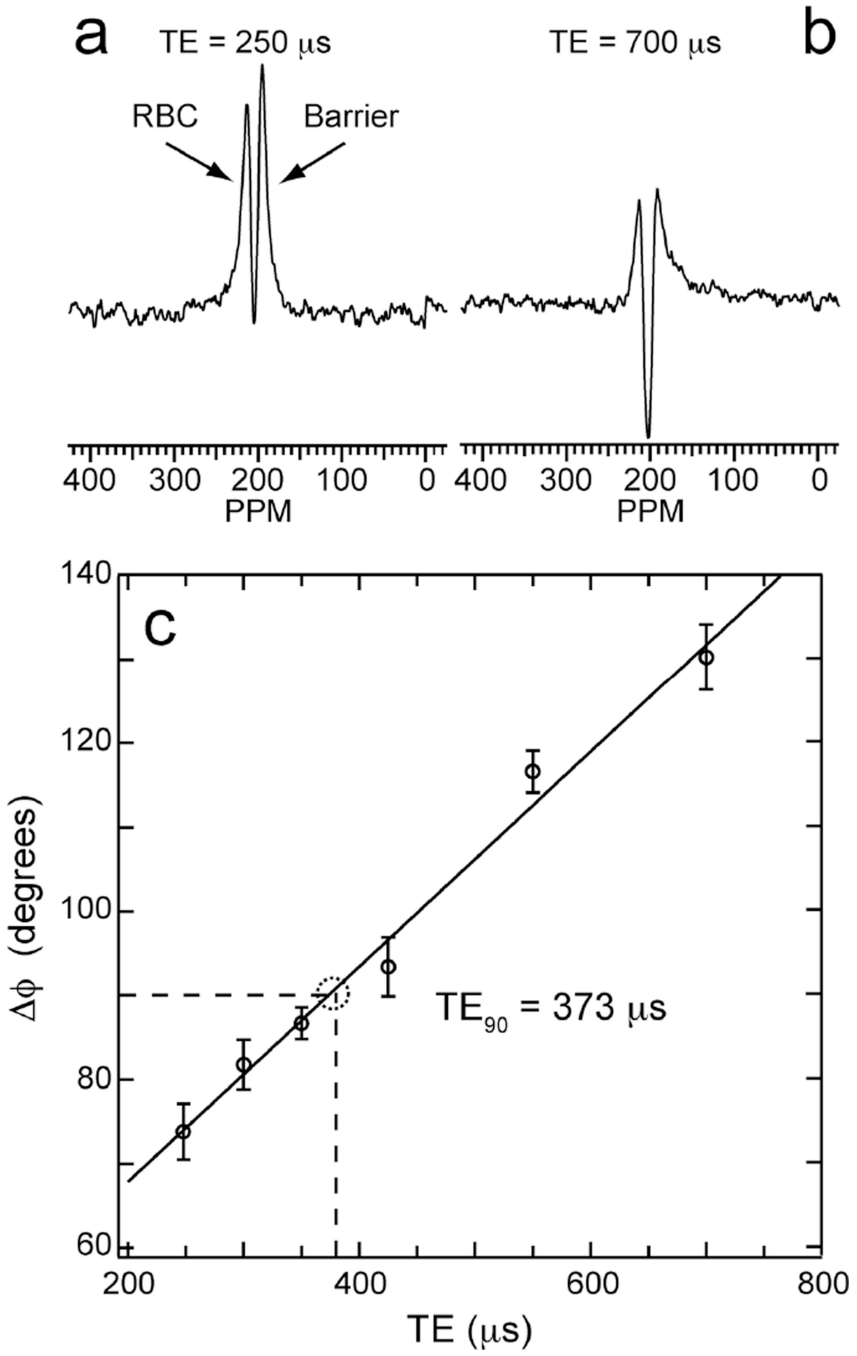


**Figure 1.**

Empirical determination of the nominal echo time required to accumulate a 90° phase difference ($TE_{90}$) between $^{129}Xe$ dissolved in the red bloods cells (RBC) and the barrier tissues (blood plasma and lung parenchyma). **a**) Dissolved $^{129}Xe$ spectrum at TE =250 μs. **b**) Dissolved $^{129}Xe$ spectrum processed identically, but at TE = 700 μs. **c**) Dissolved$^{129}Xe$ phase evolution as a function of time. Linear regression (black line) shows that 90° phase difference is achieved at TE = 373 μs rather than the ~730 μs expected from$\boldsymbol{TE_{90} = 1/(4\Delta F)}$.

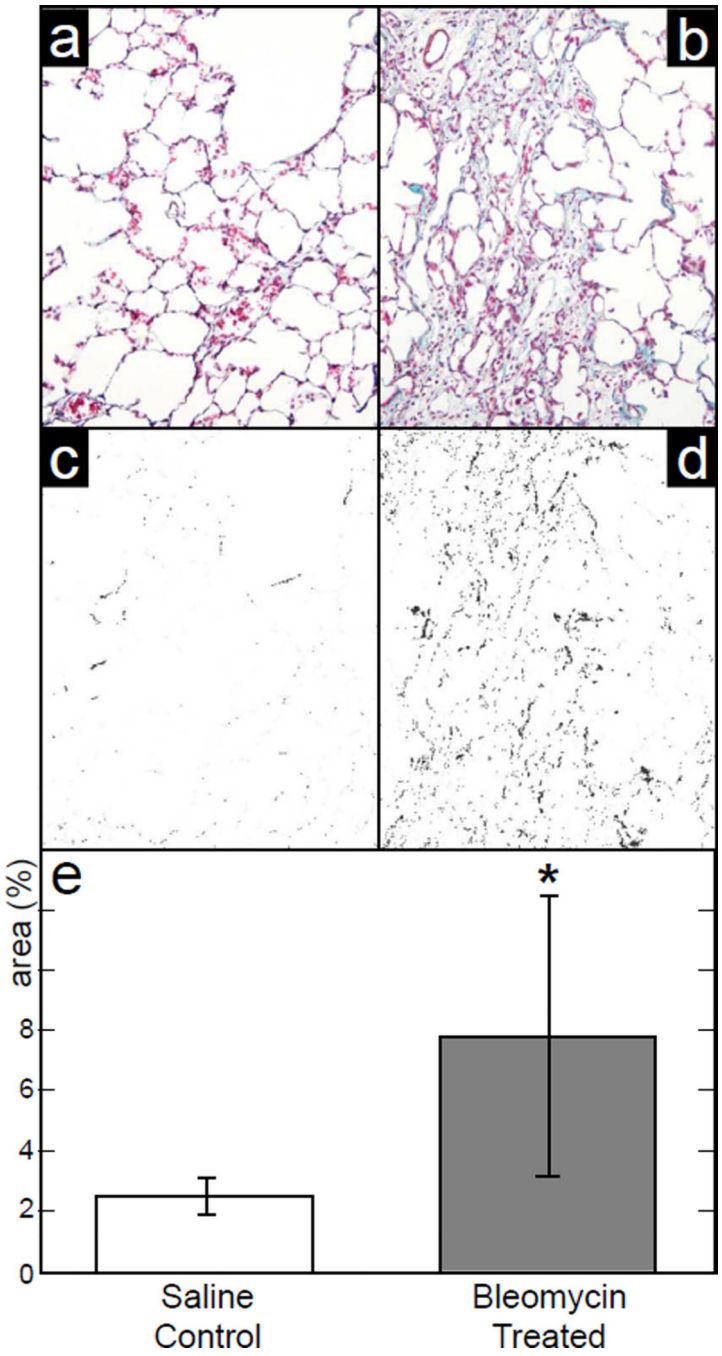


**Figure 2.**

Histological assessment of fibrotic injury. (**a**) Masson's Trichrome stained lung tissue from a saline-treated control rat. Alveolar walls are thin and intact; little collagen (blue-stained tissue) is present. (**b**) Identically stained tissue from a Bleomycin-treated rat. Thickened alveolar walls and collagen accumulation indicate fibrotic injury. (**c**) Image from (a) color thresholded such than only collagen containing areas are retained. (**d**) Color-thresholded image displaying the collagen-containing area from (b). (**e**) Comparison of percent average collagen-containing area from saline- and Bleomycin-treated groups. The percentage of

collagen-containing area was significantly greater in the Bleomycin-treated group relative to the saline control group ($P = 0.008$).

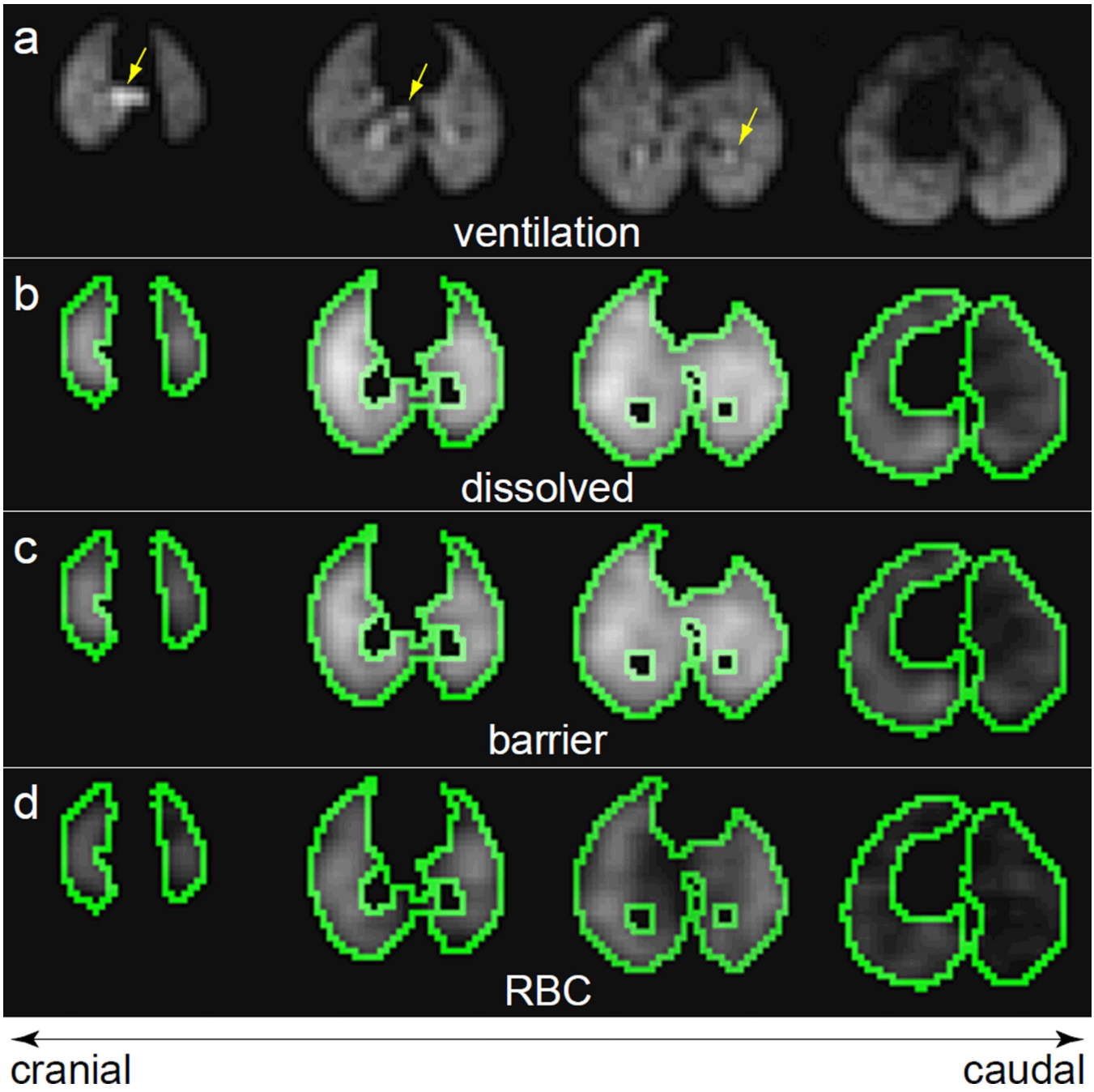


**Figure 3.**

Axial slices from3D HP $^{129}$Xe MR images of a control rat, which received a saline treatment in the right lung. (**a**) Ventilation image. Arrows indicate the location of the larger airways. The corresponding slices from the total dissolved $^{129}$Xe image (**b**), barrier tissue image, (**c**) and RBC image (**d**) are also shown. The green outlines depict the edges of the mask used to confine data analysis to the ventilated regions of the lung parenchyma.

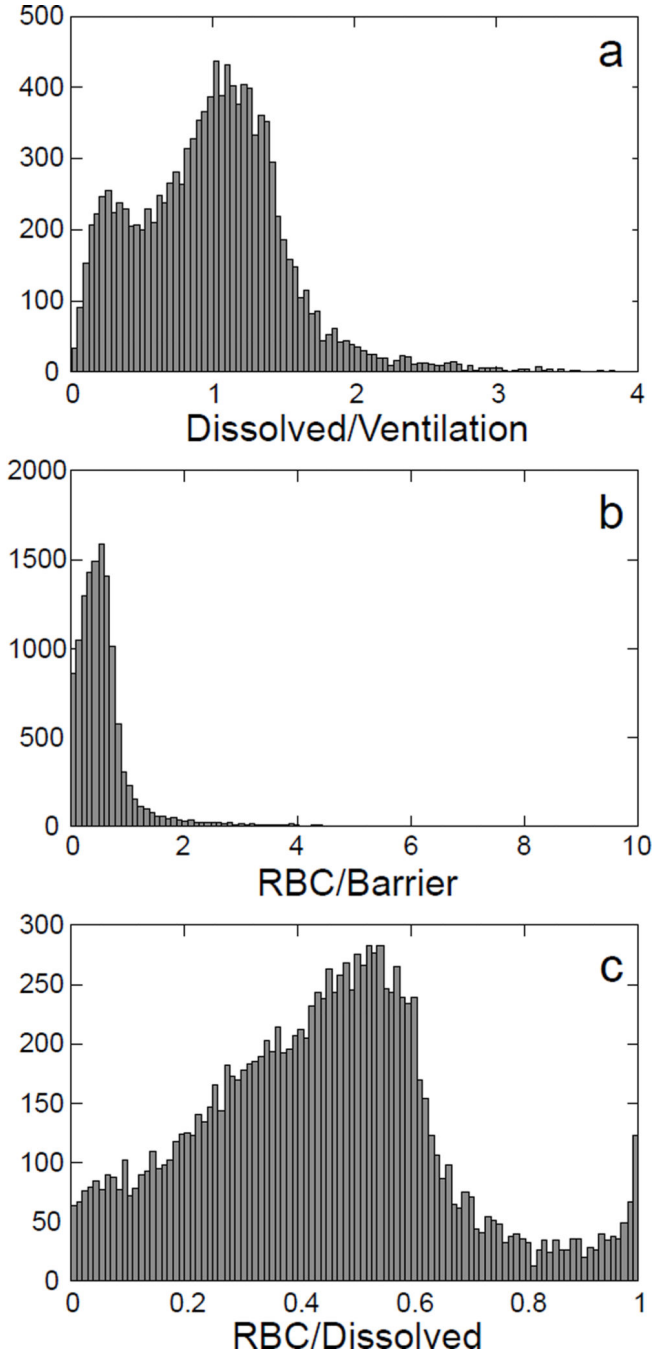


**Figure 4.**

Histograms displaying the distributions of dissolved $^{129}$Xe signal from a saline-treated control rat. (**a**) Dissolved-to-ventilation (i.e., gas-transfer) ratio distribution, showing a mean near 1. (**b**) RBC-to-barrier ratio, displaying a highly left-skewed distribution. (**c**) RBC-to-dissolved ratio, displaying a relatively uniform distribution, with values arranging from 0 to 1.

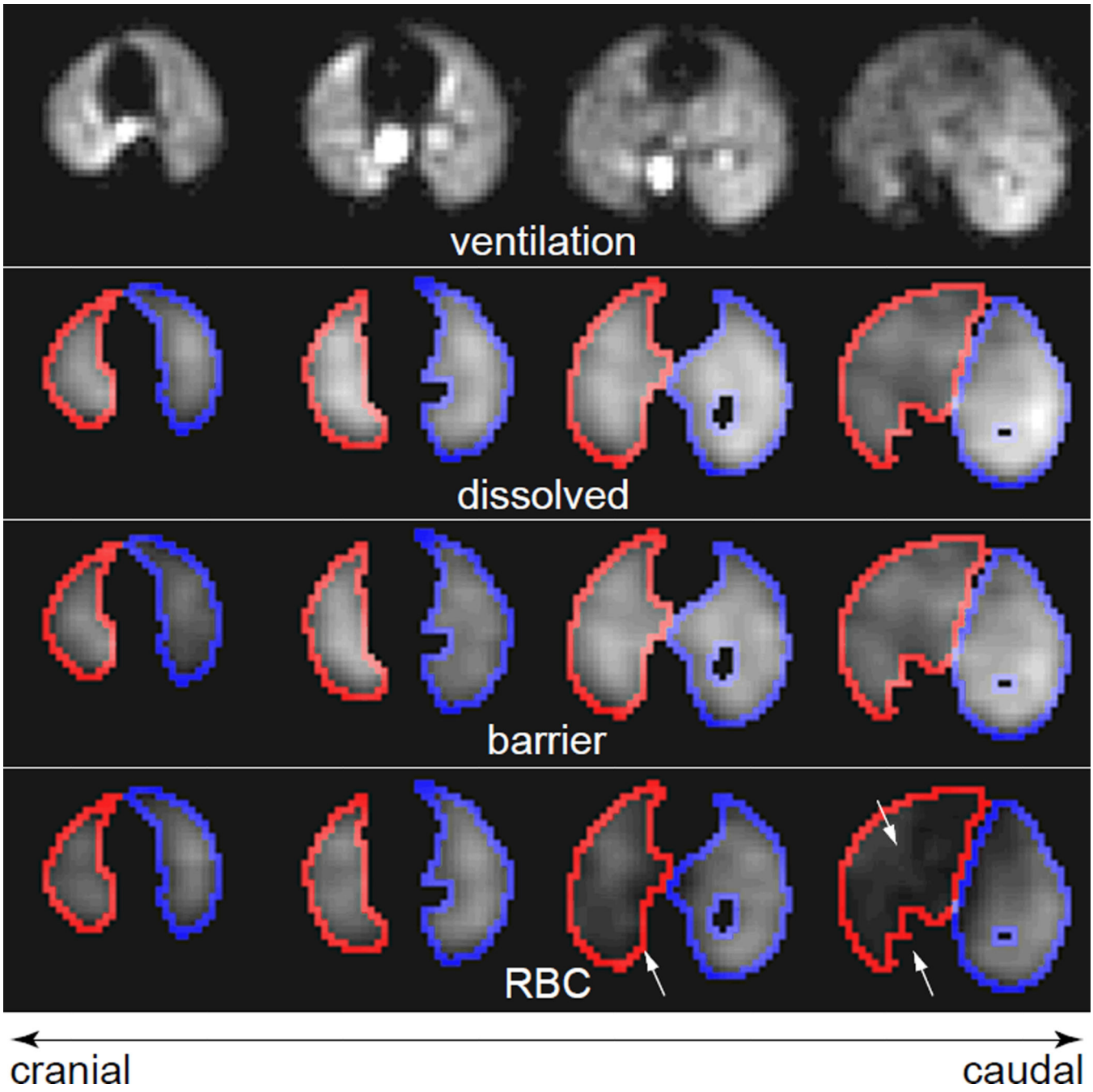


**Figure 5.**

Axial slices from a 3D HP $^{129}$Xe MR images of a Bleomycin-treated rat. (**a**) Ventilation image. Again, the lung parenchyma is reasonably well ventilated. Also shown are the corresponding slices from the (**b**) total dissolved $^{129}$Xe image, (**c**) barrier tissue image, and (**d**) RBC image. Outlines depict the edges of the mask used to confine data analysis to the injured (right, red) and uninjured (left, blue) lung. Arrows indicate regions of reduced RBC signal within the injured lung.

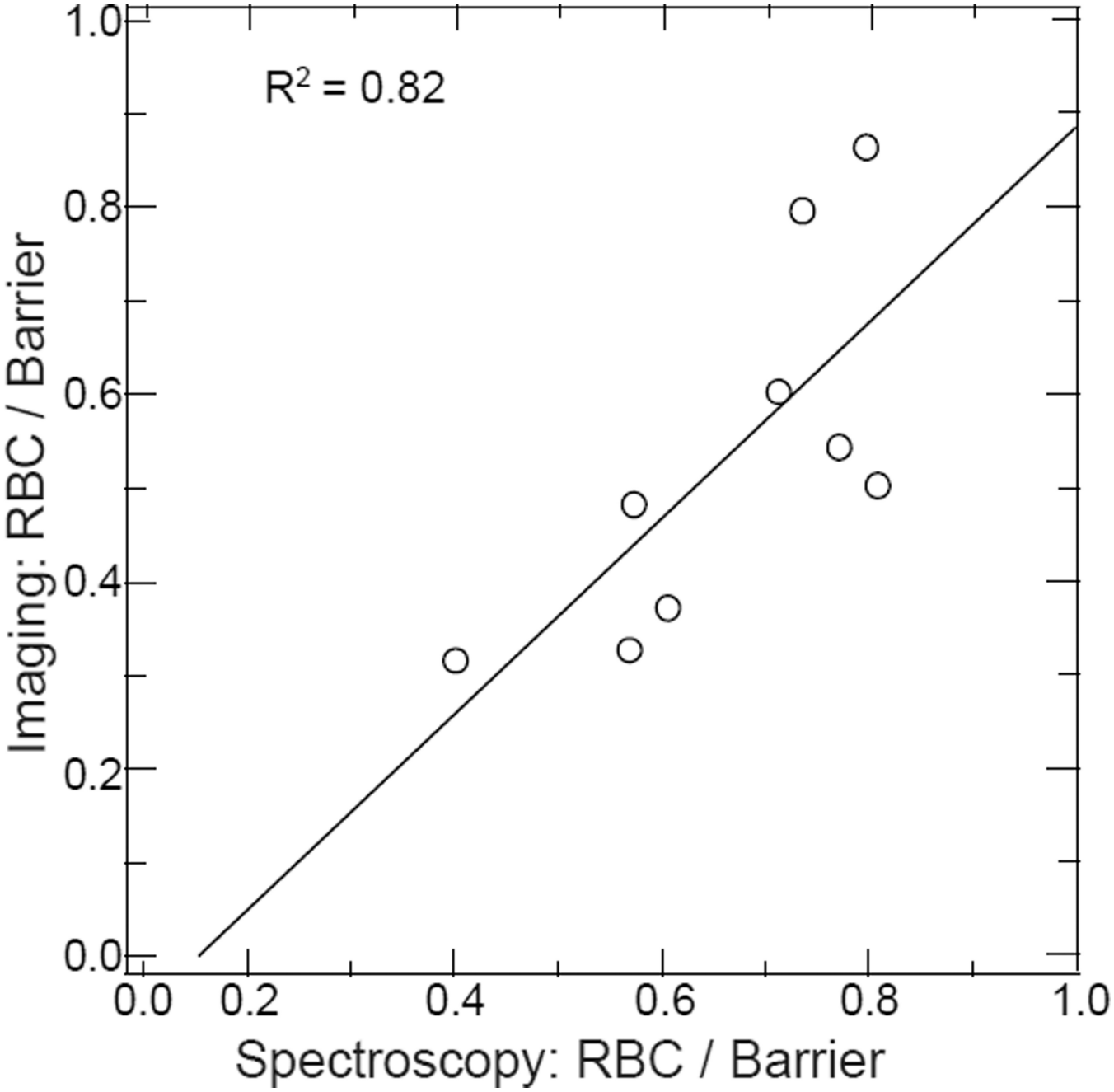


**Figure 6.**

Correlation of total RBC to total barrier tissue ratio. Data are the RBC-to-barrier tissue signal ratios obtained via whole-lung spectroscopy (x-axis) and 1-point Dixon imaging (y-axis). The solid line is a linear, least squares fit of the data, and indicates that the two metric of total gas uptake are well correlated ($R^2$ = 0.82).

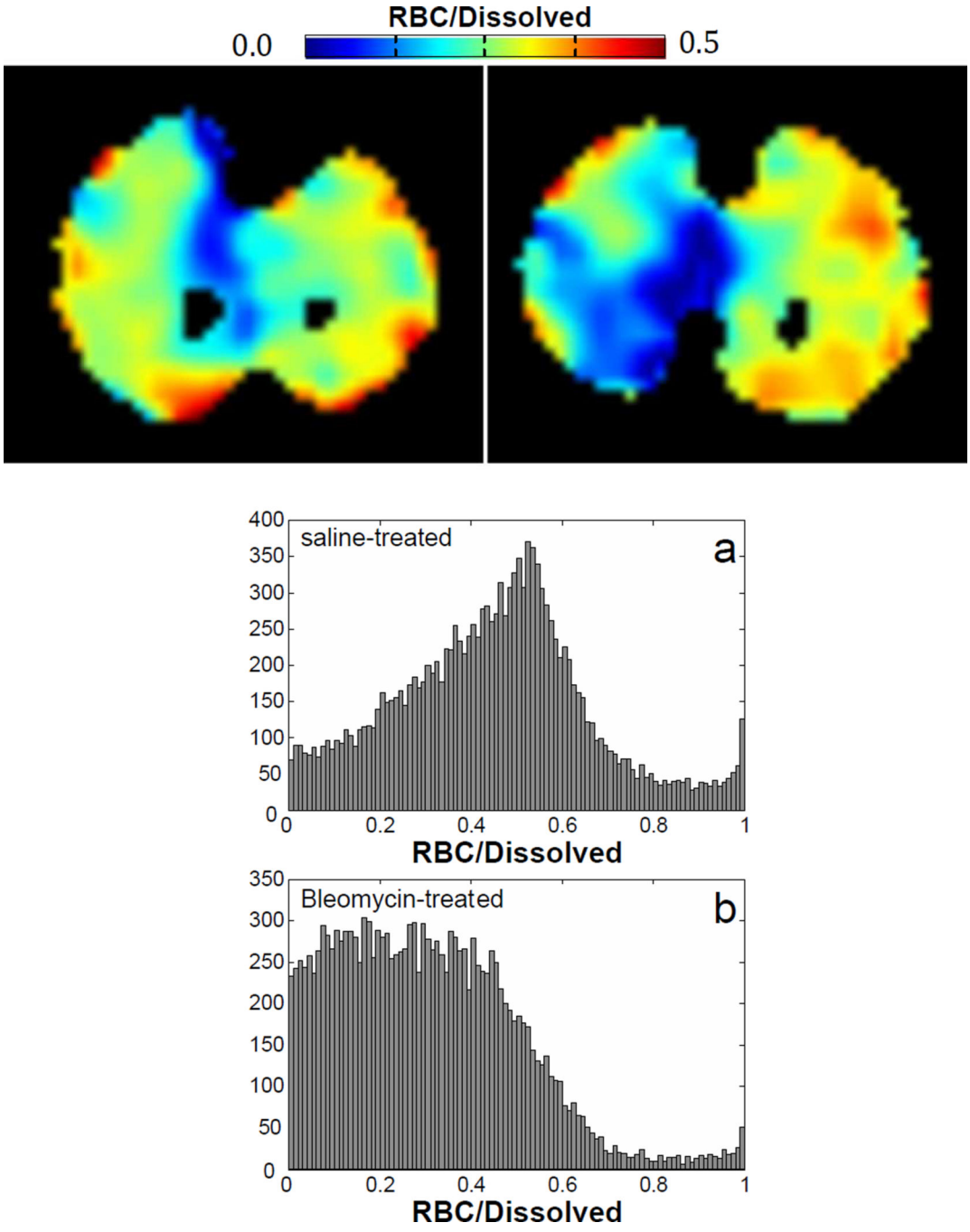


**Figure 7.**

(a), (b) Axial slices from the RBC-to-dissolved maps of a saline control animal (a) and a bleomycin-treated animal (b). (c), (d) Corresponding whole lung, RBC-to-dissolved 129Xe histograms from the saline control animal (c) and bleomycin-treated animal (d) shown in (a) and (b), respectively. The distribution displayed by the control animal is quantitatively similar to that displayed in Figure 4c). The distributions from the bleomycin-treated animals, however, display markedly different character, reflecting reduced 129Xe transfer to RBCs and substantial regional variability.

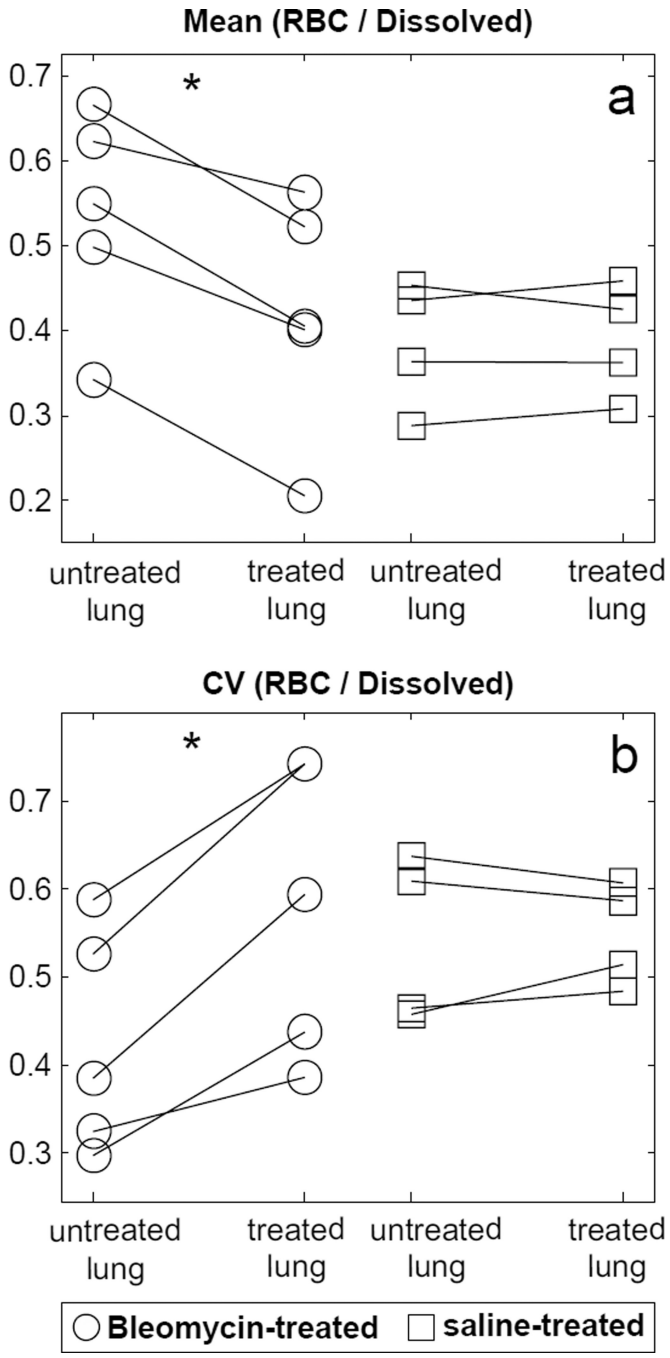


**Figure 8.**

Dissolved signal distribution in treated versus untreated lungs. (**a**) Mean RBC-to-dissolved ratio. In the Bleomycin-treated group, the mean RBC-to-dissolved ratio was significantly lower than in the untreated lung (P = 0.03), but no significant difference was observed in the saline-treated control group between the treated and untreated lung (P = 0.31). (**b**) Coefficient of variation (CV) for the RBC-to-dissolved ratio shown in (a). A significantly

higher treated-lung CV was observed in the Bleomycin group (P = 0.03), but not in the saline control group (P = 0.56).

**Table 1**

Whole-lung comparisons of Bleomycin- and saline-treated groups. [a]

| | Collagen (% area) | Dissolved / Ventilation | RBC / Barrier | | RBC / Dissolved | Spectroscopy | Imaging |
|---|---|---|---|---|---|---|---|
| **Bleomycin** | 7.8±4.7 | 1.03±0.03 | 0.72±0.09 | 0.63±0.2 | 0.48±0.13 | | |
| **Treated** | | | | | | | |
| **Saline** | 2.5±0.2 | 1.02±0.02 | 0.60±0.17 | 0.42±09 | 0.39±0.08 | | |
| **Control** | | | | | | | |
| **P-value** | 0.008 | 0.73 | 0.56 | 0.11 | 0.29 | | |

[a] Population mean ± standard deviation.